J. Fluid Mech. (2011), *vol.* 672, *pp.* 545–569.
doi:10.1017/S0022112010006142

Acoustic–convective mode conversion in an aerofoil cascade

P. PALIES[1]†, D. DUROX[1], T. SCHULLER[1] AND S. CANDEL[1,2]

[1]EM2C Laboratory, École Centrale Paris and CNRS, Grande Voie des Vignes, 92295 Châtenay-Malabry, France

[2]Institut Universitaire de France, 103 Boulevard Saint-Michel, 75 005 Paris, France

(Received 15 March 2010; revised 24 November 2010; accepted 25 November 2010; first published online 14 February 2011)

When an acoustic wave impinges on an aerofoil cascade, a convective vorticity mode is generated giving rise to transverse velocity perturbations. This mode conversion process is investigated to explain the flow dynamics observed when swirlers are submitted to incident acoustic disturbances. The phenomenon is first studied in the case of a two-dimensional aerofoil cascade using a model derived from an actuator disk theory. The model is simplified to deal with low-Mach-number flows. The velocity field on the downstream side of the cascade features two components, an axial perturbation associated with the transmitted acoustic wave and a transverse disturbance corresponding to the vorticity wave generated at the cascade trailing edge. The model provides the amplitude of both components and defines their phase shift. Numerical simulations are carried out in a second stage to validate this model in the case of a cascade operating at a low Reynolds number $Re_c = 2700$ based on the chord length. Space–time diagrams of velocity perturbations deduced from these simulations are used to retrieve the two types of modes. Experiments are then carried out in the case of an axial swirler placed in a cylindrical duct and submitted to plane acoustic waves emitted on the upstream side of the swirler. The amplitude and phase of the two velocity components measured in the axial and azimuthal directions are found to be in good agreement with theoretical estimates and with numerical calculations. This analysis is motivated by combustion dynamics observed in flames stabilized by aerodynamic swirlers in continuous combustors.

Key words: acoustics, aerodynamics, compressible flows

1. Introduction

Mode conversion is a mechanism where one type of propagating disturbance generates another type of wave. This involves convective modes (entropy and vorticity) and acoustic modes and takes place in many situations in fluid dynamics. The present investigation is concerned with one such mechanism whereby an acoustic wave is incident on an aerofoil cascade producing a vorticity wave in the downstream flow. At this point, it is worth putting this problem in perspective by reviewing configurations of fundamental and practical interest where mode conversion is important.

In figure 1(*a*), entropy waves, generally hot spots, convected through a nozzle generate acoustic pressure waves which are radiated to the far field. This mechanism

† Email address for correspondence: paul.palies@em2c.ecp.fr

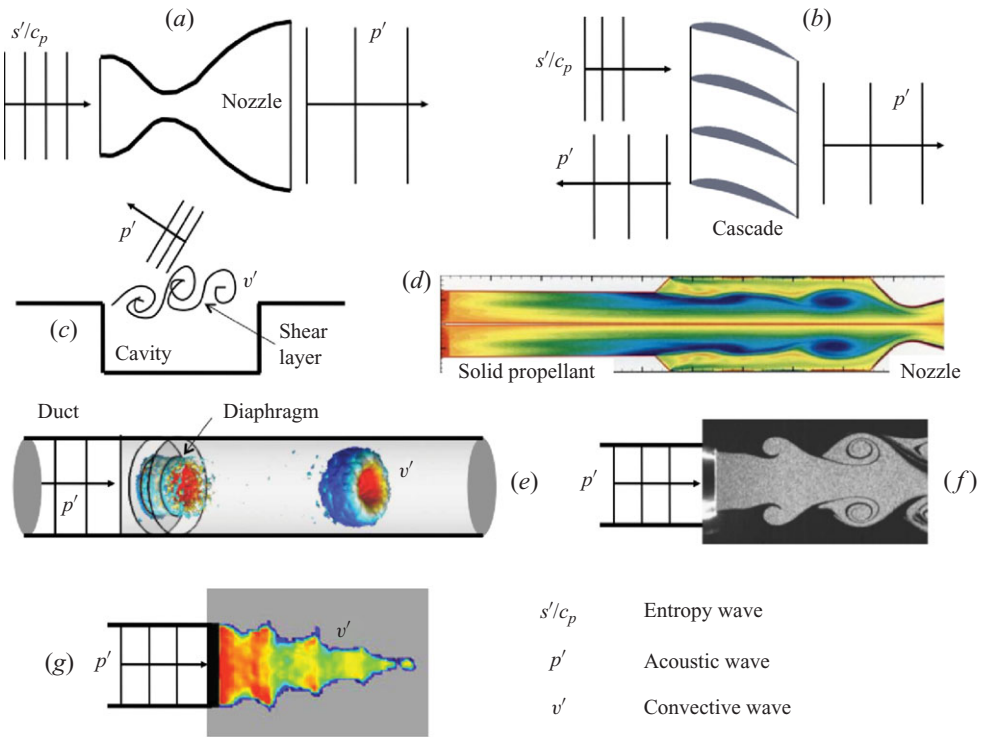

FIGURE 1. Review of mode conversion mechanisms. (*a*) Entropy waves, generally hot spots, convected through a nozzle generate acoustic pressure waves which are radiated to the far field. (*b*) Entropy waves impinging on a blade row. (*c*) Vortices shed from the upstream side of a cavity exposed to a uniform flow. (*d*) Vortices shed from baffles separating the propellant segments and protruding in the gas stream or from the edge of the propellant block. (*e*) Acoustic waves are impinging the diaphragm and vortices are then generated. (*f*) Modulated jet exhausted from a nozzle or a channel into a quiescent atmosphere. (*g*) Conical flame submitted to acoustic modulations.

designated as 'entropy noise' or indirect combustion noise initially considered by Candel (1972) and Marble & Candel (1977) has been examined extensively in relation with aeroacoustic applications by Morfey (1973*a*), Ffwocs-Williams & Howe (1975), Howe (1975), Bake *et al.* (2009) and Leyko, Nicoud & Poinsot (2009). A related problem considered by Cumpsty & Marble (1977*a*) is that of entropy waves impinging on a blade row sketched in figure 1(*b*). The cascade acts like a nozzle and the incident entropy waves are accelerated in the flow generating acoustic waves propagating in the upstream and downstream directions. This again constitutes a source of core noise in gas turbines studied by Cumpsty & Marble (1977*b*). In the third configuration shown in figure 1(*c*), the coupling results from vortices shed from the upstream side of a cavity exposed to a uniform flow. The vortices impinge on the downstream cavity lip and generate acoustic waves which, in turn, synchronize the vortex shedding mechanism at the cavity leading edge (see, for example, the review by Rockwell & Naudascher 1979). Characteristic frequencies can be estimated with an expression due to Rossiter (1964). A related problem found in solid propellant rocket engines is shown in figure 1(*d*). Here, vortices are shed from baffles separating the propellant segments and protruding in the gas stream or from the edge of the propellant block as exemplified in this subfigure. The vortices impinge on the nozzle radiating an acoustic wave which may

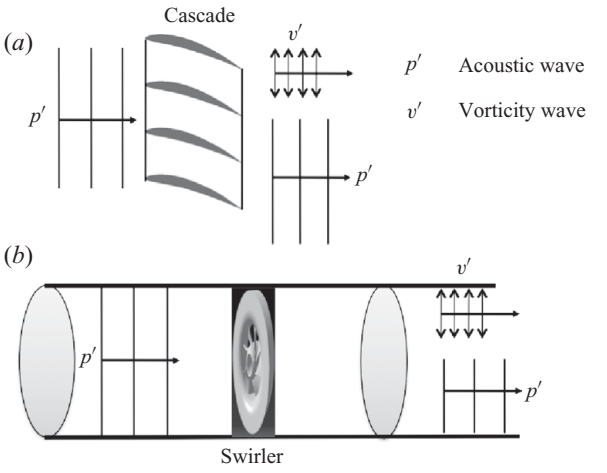

FIGURE 2. Mode conversion mechanisms studied in the present work. (*a*) Acoustic waves impinging on an aerofoil cascade. (*b*) Acoustic waves impinging on a swirler in a duct.

couple with the vortex shedding mechanism giving rise to self-sustained oscillations. In solid rocket engines, this mechanism is responsible for troublesome thrust oscillations augmenting the vibrational levels on the payload as studied by Dotson, Koshigoe & Pace (1997). A simplified version of the previous case is shown in figure 1(*e*) where a diaphragm blocks the flow in a channel. When an acoustic wave impinges on this constriction, vortices are generated. The mode conversion process taking place in this geometry is studied in a recent article by Noiray *et al.* (2009). Another situation of interest is that of a jet exhausted from a nozzle or a channel into a quiescent atmosphere as shown in figure 1(*f*). An acoustic wave propagating in the upstream flow and interacting with a channel exhaust produces a convective mode in the free jet when the Strouhal number is sufficiently low meaning that the oscillation is in the low-frequency range. This process has received considerable attention in the past and is the subject of a classical article by Crow & Champagne (1971). Birbaud *et al.* (2007) provide many additional references and map the various modes of interactions in a diagram. A related process takes place in a flame stabilized on a burner equipped with a driver unit as in figure 1(*g*). In the low-frequency range, the acoustic wave is transformed into a convective mode which modulates the flame. This type of mode conversion has been studied, for example, by De Soete (1964), Boyer & Quinard (1990), Baillot, Durox & Prudhomme (1992), Bourhela & Baillot (1998), Schuller, Durox & Candel (2003), Birbaud, Durox & Candel (2006), Kornilov *et al.* (2007) and Shanbhogue *et al.* (2009).

The present article is concerned with the problem shown in figures 2(*a*) and 2(*b*). An acoustic wave impinges on an aerofoil cascade or a swirler placed in a duct. The motivation for this analysis lies in the domain of combustion dynamics. In many combustors operating in a continuous mode, the flame is stabilized in a swirling flow generated by axial or radial vanes. Typical gas turbine combustors rely on radial swirlers which impart rotation to the incoming air producing an inner recirculation zone filled with hot gases and anchoring the flame in the vicinity of the injection plane. Under unstable operation coupling acoustics and combustion, the swirlers are submitted to incident acoustic perturbations. It is interesting to examine this situation and specifically analyse the possible generation of a vorticity wave and the associated velocity perturbations on the downstream side of the swirler. At this point, it is

worth briefly reviewing the literature dealing with the interaction of perturbations with blade rows. This problem covered in the classical textbooks of Horlock (1978) and Greitzer, Tan & Graf (2004) has been extensively investigated in the domain of turbomachinery, for example, by Kaji & Okazaki (1970), Koch (1971) and Morfey (1973*b*) in early works and more recently by Peake & Kerschen (1997) and Glegg (1999). It is important because such interactions induce fluctuating forces on the blades generating noise and undesirable vibrations. Conversion of entropy fluctuations by a cascade has been worked out analytically by Cumpsty & Marble (1977*b*) and was pursued by Cumpsty (1979). It is shown that the interaction gives rise to acoustic pressure waves. These studies are used as starting points of the model developed in the present article. Most of these studies consider high-Mach-number flows found in axial compressors or turbines, the case of low Mach flows is less well documented.

The response of a cascade to unsteady perturbations can be studied with numerical simulations as exemplified by Paynter (1997). The case of swirlers interacting with acoustic perturbations has recently been examined by Wang & Yang (2005) using large eddy simulations (LES). Consequences on the dynamics of swirling flames are discussed in a recent review by Huang & Yang (2009). It is deduced from simulations that axial and azimuthal velocity disturbances propagate at different velocities on the downstream side of the swirler. This is also inferred by Hirsch *et al.* (2005) and Komarek & Polifke (2010). While the presence of the convective component is recognized by these authors, there are no direct measurements of the axial and azimuthal velocity components which support this conclusion and no theoretical attempt is made to estimate the respective levels of the various perturbations, except perhaps in a study carried out by Sajben & Said (2001) where the strength of the vorticity wave is estimated.

This article is organized as follows. A theoretical formulation is first derived from the analysis of Cumpsty & Marble (1977*b*) to deal with situations where the Mach number is low corresponding to standard operation of swirlers (§ 2). The blade row is assumed to operate in the low-velocity range and interacts with an incident acoustic wave giving rise to a perturbed velocity field downstream of the cascade. Amplitudes of the downstream perturbations are determined. The model is derived in two dimensions, a standard assumption used in turbomachinery analysis, where the flow is described on a median cylindrical surface located at equal distances from hub and tip. The underlying equations are based on an actuator disk description. Numerical simulations are carried out with a Navier–Stokes unsteady flow solver (§ 3). Simulations are performed in a two dimensional (2D) cascade which is consistent with the 2D theory. The modulation-free flow established in a group of aerofoils is obtained in a first step. In this simulation, the wakes formed at the aerofoil trailing edges give rise to a shear layer instability which develop into a Kármán street of vortices. The flow is then modulated by an axial acoustic wave which propagates towards the cascade. Two modulation frequencies are considered $f = 60$ and $f = 100\,\mathrm{Hz}$ corresponding to two Strouhal numbers based on the chord length, respectively equal to 0.15 and 0.25 for two amplitudes of the inlet velocity fluctuation $u'_\infty = 0.1\,\mathrm{m\,s^{-1}}$ and $u'_\infty = 1\,\mathrm{m\,s^{-1}}$. These simulations are used to extract the velocity component amplitudes. Space–time diagrams are plotted highlighting the axial and azimuthal modes of propagation. The problem is then examined experimentally by making use of a ducted swirler submitted to a plane acoustic wave (§ 4). This axisymmetric geometry is easier to consider for the experiments. The situation is close to that found in turbomachinery analysis where calculations are carried out in 2D cascade configurations while the real geometry has a rotational symmetry. The objective is not so much to reproduce simulations through

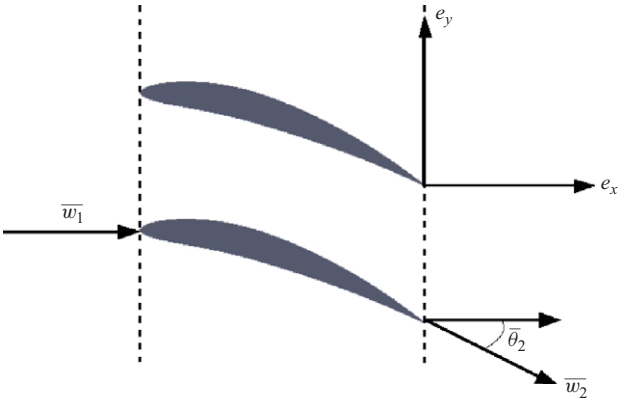

FIGURE 3. Geometry of the aerofoils cascade.

an experiment but to reveal a mechanism and for this one may use the geometry which is easiest to explore. The perturbed velocity field on the downstream side of the swirler is characterized and these data are compared with theoretical estimates and numerical calculations (§ 5).

2. Theoretical model

This analysis is concerned with the interaction taking place between a swirler and incident acoustic perturbations. This problem is easier to tackle theoretically by considering the 2D geometry of a cascade as plotted in figure 3. The incoming flow velocity $\overline{w}_1$ is oriented in the axial direction while the outgoing flow $\overline{w}_2$ makes an angle $\overline{\theta}_2$ with respect to the axis. One assumes that the flow velocities remain in the low-Mach-number range. The characteristic size of the cascade (the blade chord) is small compared to the acoustic wavelengths considered. The ratio is typically of the order of 0.01. One may then consider that it is compact with respect to the incident wave field and use an actuator disk to represent the blade row. The swirler can then be treated as a discontinuity for these perturbations and operates like an actuator disk.

To relate perturbations on the upstream and downstream sides of this cascade, one may use jump conditions provided by Cumpsty & Marble (1977*b*) which are adapted to a low-Mach-number flow:

$$s'_1 = s'_2, \tag{2.1}$$

$$\frac{\rho'_1}{\overline{\rho}_1} + \frac{w'_1}{\overline{w}_1} - \theta'_1 \tan\overline{\theta}_1 = \frac{\rho'_2}{\overline{\rho}_2} + \frac{w'_2}{\overline{w}_2} - \theta'_2 \tan\overline{\theta}_2, \tag{2.2}$$

$$\frac{p'_1}{\gamma\overline{p}_1} + \frac{s'_1}{(\gamma-1)c_p} = \frac{p'_2}{\gamma\overline{p}_2} + \frac{s'_2}{(\gamma-1)c_p}, \tag{2.3}$$

where s' is the entropy fluctuation and $\rho'/\overline{\rho}$ the relative density fluctuation. Subscripts 1 and 2 refer to inlet and outlet of the cascade vanes. The ratios $w'_1/\overline{w}_1$ and $w'_2/\overline{w}_2$ are the relative velocity fluctuations on each side of the cascade, θ'_1 is the fluctuation of the angle of incidence θ_1, θ'_2 is the fluctuation of the angle θ_2 at the trailing edge, p' refers to the fluctuation in pressure, γ is the specific heat ratio and c_p is the specific heat of the working fluid. At the trailing edge, the Kutta condition implies that the flow should leave the blade in a direction tangent to the mean camber line so that

the perturbation angle vanishes $\theta_2' = 0$. In region 1, the pressure field is formed by incident and reflected acoustic waves which are taken as plane waves propagating in the axial direction:

$$p_1' = A \exp \mathrm{i}(kx - \omega t) + AR \exp \mathrm{i}(-kx - \omega t), \tag{2.4}$$

where A is the amplitude of the incident acoustic wave, R is the reflection coefficient of this wave and $k = \omega/c$ designates the acoustic wavenumber. The velocity fluctuation corresponding to this field is expressed as

$$u_1' = \frac{A}{\overline{\rho}_1 \overline{c}_1} \exp \mathrm{i}(kx - \omega t) - \frac{AR}{\overline{\rho}_1 \overline{c}_1} \exp \mathrm{i}(-kx - \omega t), \tag{2.5}$$

where $\overline{\rho}_1$ and $\overline{c}_1$ are the density and the speed of sound in region 1. It is assumed in the present analysis that the mean density and speed of sound are the same on both sides of the swirler : $\overline{\rho}_1 = \overline{\rho}_2 = \overline{\rho}$ and $\overline{c}_1 = \overline{c}_2 = \overline{c}$. In region 2, the transmitted acoustic pressure also propagating in the axial direction can be written as

$$p_2' = AT \exp \mathrm{i}(kx - \omega t), \tag{2.6}$$

where T is the transmission coefficient and the corresponding acoustic velocity component is (subscript a):

$$(u_2')_a = \frac{AT}{\overline{\rho}\,\overline{c}} \exp \mathrm{i}(kx - \omega t). \tag{2.7}$$

A vorticity wave (subscript v) is also generated at the swirler. This is required to satisfy the set of jump conditions. The incident acoustic field has a wavevector which is perpendicular to the actuator disk. This field of plane waves and those corresponding to the reflected and transmitted acoustic waves have a zero wavevector projection in the transverse direction. As a consequence, the vorticity wave must also have a zero wavevector projection in the transverse direction to be compatible with the other wave fields. The vorticity wave corresponds to a convective velocity fluctuation which is transverse to the direction of propagation. There are no velocity perturbations in the x-direction to satisfy conservation of mass. The vorticity wave must then have a zero wavenumber in the transverse direction y and it is convected by the mean flow in the replace by x-direction with a velocity $\overline{u}_2 = \overline{w}_2 \cos \overline{\theta}_2$ which is also equivalent to $\overline{v}_2 = \overline{u}_2 \tan \overline{\theta}_2$. This wave comprises a single velocity component of amplitude B in the transverse direction:

$$(v_2')_v = B \exp \mathrm{i}\left[\frac{\omega x}{\overline{w}_2 \cos \overline{\theta}_2} - \omega t\right]. \tag{2.8}$$

Velocity perturbations on the downstream side of the swirler have the following components:

$$\boldsymbol{w}_2' = (u_2')_a \boldsymbol{e}_x + (v_2')_v \boldsymbol{e}_y. \tag{2.9}$$

In what follows, one may drop indices a and v but it is important to remember that the axial and transverse velocity components, respectively correspond to an acoustic wave propagating at the speed of sound $\overline{c}$ and to a vorticity wave convected at the flow velocity $\overline{u}_2 = \overline{w}_2 \cos \overline{\theta}_2$ in the axial direction. It is interesting to determine fluctuations in the modulus of the downstream flow velocity $\boldsymbol{w}_2' = u_2' \boldsymbol{e}_x + v_2' \boldsymbol{e}_y$ and in the angle θ_2'. We begin with

$$\overline{w}_2 + w_2' = \left[(\overline{u}_2 + u_2')^2 + (\overline{v}_2 + v_2')^2\right]^{\frac{1}{2}}. \tag{2.10}$$

Neglecting second-order terms, this last expression can be written as

$$\overline{w}_2 + w_2' = \left(\overline{u}_2^2 + \overline{v}_2^2\right)^{\frac{1}{2}} \left[1 + 2\frac{\left(\overline{u}_2 u_2' + \overline{v}_2 v_2'\right)}{\overline{u}_2^2 + \overline{v}_2^2}\right]^{\frac{1}{2}}. \tag{2.11}$$

Expanding the square root to first-order, one finds

$$\overline{w}_2 + w_2' = \overline{w}_2 \left[1 + \frac{\left(\overline{u}_2 u_2' + \overline{v}_2 v_2'\right)}{\overline{w}_2^2}\right] \tag{2.12}$$

and the fluctuation in modulus may be written as

$$w_2' = \frac{\overline{u}_2}{\overline{w}_2} u_2' + \frac{\overline{v}_2}{\overline{w}_2} v_2'. \tag{2.13}$$

This can be cast in the following form for w_2':

$$w_2' = \cos\overline{\theta}_2 u_2' + \sin\overline{\theta}_2 v_2'. \tag{2.14}$$

Some straightforward calculations also lead to

$$\theta_2' = \sin\overline{\theta}_2 \cos\overline{\theta}_2 \left[\frac{v_2'}{\overline{v}_2} - \frac{u_2'}{\overline{u}_2}\right]. \tag{2.15}$$

Noting that the change in pressure and density across the swirler is small ($\overline{p}_1 \simeq \overline{p}_2$, $\overline{\rho}_1 \simeq \overline{\rho}_2$), one easily deduces from the previous set of jump conditions that:

$$p_1' = p_2', \tag{2.16}$$

$$\frac{w_1'}{\overline{w}_1} - \theta_1' \tan\overline{\theta}_1 = \frac{w_2'}{\overline{w}_2} - \theta_2' \tan\overline{\theta}_2, \tag{2.17}$$

Now, the fluctuation in angle on the downstream side of the swirler must vanish to satisfy the unsteady Kutta condition $\theta_2' = 0$. Since fluctuations on the upstream side are only axial $w_1' = u_1'$, one deduces that there are no angular fluctuations at the leading edge $\theta_1' = 0$. The jump conditions for the perturbations simplify to

$$p_1' = p_2', \tag{2.18}$$

$$\frac{u_1'}{\overline{w}_1} = \frac{u_2' \cos\overline{\theta}_2 + v_2' \sin\overline{\theta}_2.}{\overline{w}_2} \tag{2.19}$$

Inserting (2.4)–(2.8) in these last expressions, one obtains

$$A(1 + R) = T, \tag{2.20}$$

$$\frac{A}{\overline{\rho}\,\overline{c}} \frac{1}{\overline{w}_1}(1 - R) = \frac{AT}{\overline{\rho}\,\overline{c}} \frac{1}{\overline{w}_2} \cos\overline{\theta}_2 + \frac{B \sin\overline{\theta}_2}{\overline{w}_2}. \tag{2.21}$$

Noting that the steady state mass balance requires that $\overline{w}_1 = \overline{w}_2 \cos\overline{\theta}_2$, the previous expression becomes

$$A(1 - R) = \cos^2\overline{\theta}_2 AT + \overline{\rho c} \sin\overline{\theta}_2 \cos\overline{\theta}_2 B. \tag{2.22}$$

From the Kutta condition $\theta_2' = 0$ (2.15), one also deduces that $v_2' = u_2' \tan\overline{\theta}_2$ which yields

$$B = \frac{AT}{\overline{\rho}\,\overline{c}} \tan\overline{\theta}_2. \tag{2.23}$$

Inserting this expression in (2.22), one obtains

$$A(1 - R) = AT. \tag{2.24}$$

This relation combined with (2.20) finally yields

$$R = 0 \qquad \text{and} \qquad T = 1. \tag{2.25}$$

Assumptions of equality of mean pressure and density on the two sides of the swirler lead to a zero reflection coefficient and to a unit value for the transmission coefficient. One also finds from this analysis that the transverse velocity is directly proportional to the axial acoustic velocity component and that $\tan\overline{\theta}_2$ defines the proportionality between these two components. This result is in agreement with previous findings by Sajben & Said (2001). It is thus possible to write the velocity components on the downstream side of the swirler in the following form:

$$u_2' = \frac{A}{\overline{\rho}\,\overline{c}} \exp \mathrm{i}\left[\frac{\omega}{\overline{c}}x - \omega t\right], \tag{2.26}$$

$$v_2' = \frac{A}{\overline{\rho}\,\overline{c}} \tan\overline{\theta}_2 \exp \mathrm{i}\left[\frac{\omega}{\overline{u}_2}x - \omega t\right]. \tag{2.27}$$

The axial velocity perturbation propagates at the speed of sound while the transverse velocity component is convected at the local flow velocity $\overline{u}_2 = \overline{w}_2 \cos\overline{\theta}_2$ in the axial direction. The previous calculations indicate that the swirler acts as a mode converter. When it is submitted to axial acoustic waves, it generates a vorticity wave which is convected by the flow in the axial direction. This convective wave is characterized by a velocity component in the transverse direction. The relative amplitude of this component is equal to the relative amplitude of the axial velocity perturbation $v_2'/\overline{v}_2 \simeq u_2'/\overline{u}_2$. These conclusions were obtained from a 2D actuator disk theory because it provides essential results without the complications encountered in a 3D configuration. Such 2D analyses are found in turbomachinery flow investigations (see, for example, Cumpsty & Marble 1977*b*). The reasoning is easy to follow in 2D because the algebra is simplified by using a well-established actuator disk framework. The analysis in 3D is more complex because of the radial velocity component. However, 3D numerical simulations carried out recently by our team in Palies *et al.* (2011) indicate that the mode conversion is confirmed and that the amplitude of the radial component is less important by an order of magnitude than the axial and azimuthal components. It is then reasonable to apply the previous results to a swirler and consider that the azimuthal velocity fluctuation can be approximately identified to the transverse component determined previously.

3. Numerical simulation

Simulation is now used to examine the unsteady flow interaction with a cascade. It is convenient to examine the process with 2D configurations. The computational requirements are reduced and calculations can be repeated. Simulations are carried out with the AVBP code (Schonfeld & Rudgyard 1999), a compressible Navier–Stokes flow solver operating on structured and unstructured meshes. AVBP solves the laminar and turbulent compressible Navier–Stokes equations in two or three space dimensions. The last effort on this code was put on modelling unsteady turbulent reactive flows motivated by activities in the field of unsteady turbulent combustion as reported by Selle *et al.* (2006) or Staffelbach *et al.* (2009). This code is used in the present context because it has a good degree of precision with a third order in space and in time discretization and suitably describes acoustic flow interactions. The filtered compressible equations exhibit subgrid-scale tensors and vectors describing the interaction between the resolved and subgrid motions.

The filtered quantity $\overline{f}$ is resolved in the numerical simulation whereas $f' = f - \overline{f}$ is the subgrid-scale part due to the unresolved flow motion. For variable density ρ, a mass-weighted Favre filtering is introduced such as

$$\overline{\rho}\,\widetilde{f} = \overline{\rho f}. \tag{3.1}$$

The balance equations for LES are obtained by filtering the instantaneous balance equations and give

$$\frac{\partial \overline{\rho}\,\widetilde{u_i}}{\partial t} + \frac{\partial}{\partial x_j}(\overline{\rho}\,\widetilde{u_i}\,\widetilde{u_j}) = -\frac{\partial}{\partial x_j}\left[\overline{P}\,\delta_{ij} - \overline{\tau_{ij}} - \overline{\tau_{ij}}^{t}\right], \tag{3.2}$$

where ρ refers to the density, u to the velocity, p to the pressure, δ the Kronecker symbol and $\overline{\tau_{ij}}$ and $\overline{\tau_{ij}}^{t}$ are, respectively the laminar and turbulent filtered stress tensors. Subscripts i, j and l refer to the three spatial dimensions while t denotes for turbulence

$$\frac{\partial \overline{\rho}\,\widetilde{E}}{\partial t} + \frac{\partial}{\partial x_j}\left(\overline{\rho}\,\widetilde{E}\,\widetilde{u_j}\right) = -\frac{\partial}{\partial x_j}\left[\overline{u_i\,(P\,\delta_{ij} - \tau_{ij})} + \overline{q_j} + \overline{q_j}^{t}\right] + \overline{\dot{\omega}_T} + \overline{Q_r}. \tag{3.3}$$

In this equation, E denotes the total energy per unit mass, $\overline{q_j}$ and $\overline{q_j}^{t}$ are, respectively the resolved filtered and the subgrid-scale heat flux vectors, $\overline{\dot{\omega}_T}$ is the chemical source term and $\overline{Q_r}$ the radiative source term. Repeated indices imply summation over this index (Einstein's rule of summation). For generality, the filtered chemical source terms ($\overline{\dot{\omega}_T}$ and $\overline{Q_r}$) are mentioned here but are not used in the present study.

In (3.2) and (3.3), one recognizes standard resolved parts including laminar stress and flux terms and an unresolved part featuring turbulent stresses and fluxes. The resolved parts are the same as those found in direct numerical simulation (DNS) but they are expressed in terms of filtered variables. In LES, the unresolved part has to be modelled. In the limiting case where the unresolved stresses and fluxes vanish, the code provides quasi-DNS solutions of the Navier–Stokes equations.

In the present analysis, the code is used in this quasi-DNS limit because the cell size in the region of interest is very small and the Reynolds number based on the chord length is low ($Re_c = 2700$). It has also been verified that standard boundary layer structures are well retrieved. Under these circumstances, the physical viscosity is much larger than the subgrid-scale viscosity. It has been checked that in the cascade and its near-field (at distances of up to 4 chords), the laminar viscosity is two orders of magnitude larger than the subgrid-scale viscosity. In order to document the effects of subgrid-scale viscosity quantitatively, the ratio of the local subgrid-scale viscosity to the laminar viscosity is plotted in figure 4. To allow more precision, 10 iso-contours of this ratio are plotted in a range extending from 0 to 0.12. The wake region is highlighted. This indicates that in this region, this ratio is, on average, around 0.02 and does not exceed 0.04. Further downstream, the level increases as the computational cell size increases and this serves to dissipate the vortex structures formed at the cascade trailing edge. The subgrid-scale stresses are only used in the present context to dissipate the vortices convected by the flow towards the outlet of the domain. This can be accomplished with a Smagorinsky model, which is used here to avoid problems linked with the passage of vortices through the downstream boundary. When the cell size is increased, dissipation by this model is augmented and the perturbations are damped in this way. The downstream part of the domain serves as a 'sponge layer' and is not used in the analysis. The acoustic motion is also well represented with the third order in space and time precision of the code. The element sizes are much

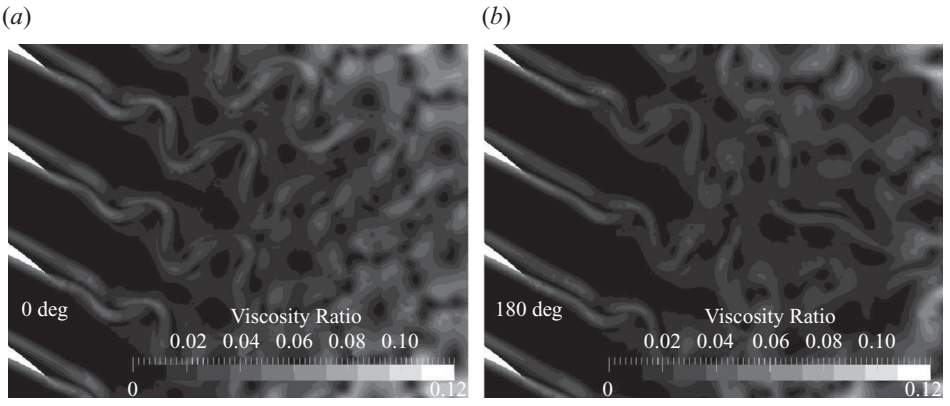

FIGURE 4. Ratio of the local subgrid-scale viscosity to the laminar viscosity in the wake region. Ten iso-contours of this ratio are plotted in a range extending from 0 to 0.12. Both results are extracted from numerical simulations with a modulation frequency $f = 60\,\mathrm{Hz}$. (*a*) Phase 0°. (*b*) Phase 180°.

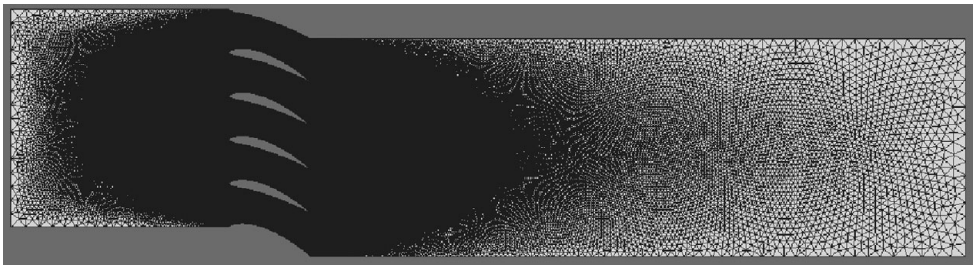

FIGURE 5. Mesh used for numerical simulations.

smaller than the wavelength and the size of the domain of interest is much smaller than the wavelength. Under these conditions, the system is compact with respect to the wavelength, the acoustic motion then corresponds to a bulk fluctuation of the flow variables and the level of dissipation and dispersion are minimal in the region of interest.

A group of five aerofoils is used to represent the cascade together with periodic boundary conditions on the upper and lower sides of the domain. The mesh shown in figure 5 comprises 450 000 cells. The total length of the computational domain is 13 cm while the transverse size is 3.1 cm corresponding, respectively to 13 and 3.1 chord lengths. Aerofoils are separated by 6 mm in the transverse direction. Several previous investigations have been carried out with the AVBP code in which tetrahedral grids have been used. Considering the growth of a laminar boundary layer over a thin flat plane, standard expressions give a thickness of nearly 1 mm at the trailing edge. Each side of the aerofoil is refined with 200 mesh points so that at least 20 points lie in the boundary layer at the trailing edge. The mesh is sufficiently refined to capture the boundary layers on the aerofoils suction and pressure sides. The minimum cell size is 0.03 mm and the typical average cell size is 0.045 mm. Time integration is explicit with a fixed time step equal to 4.5×10^{-8} s.

The air flow velocity at the numerical domain inlet is fixed to $u_\infty = 4\,\mathrm{m\,s^{-1}}$. This flow impinges on the cascade. Each aerofoil features a NACA 8411 profile which is

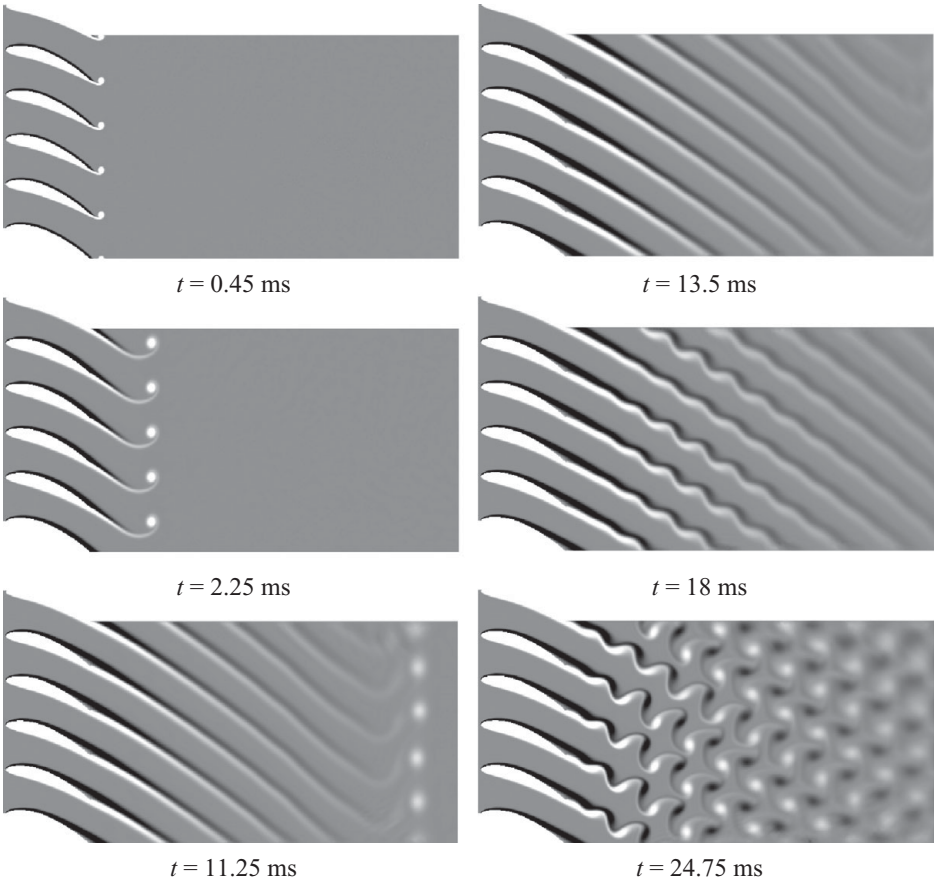

FIGURE 6. Vorticity fields of the flow in the absence of acoustic modulation. The maximum level of vorticity 5000 s^{-1} is in black while the minimum level -5000 s^{-1} is in white. The time instant of each simulation is given below each field in milliseconds. The flow dynamics goes through three stages : (i) emission of a vortex from the aerofoils trailing edges, (ii) destabilization of the wake caused by shear layer instability, (iii) fully developed Kármán vortex street.

also used to design the swirler considered in §4. The trailing edges make an angle $\overline{\theta}_2 = 25^\circ$ with the horizontal axis. The chord length of the aerofoil is $l_c = 10$ mm. No slip boundary conditions are used on the aerofoils and the upper and lower sides of the domain are periodic. Non-reflecting boundary conditions for Navier–Stokes equations are used at the computational domain inlet and outlet and this allows an easy modulation of the flow at the inlet. The outlet then behaves as a non-reflecting subsonic condition.

We first investigate the dynamics of the modulation-free flow through the cascade. There are no incident perturbations and the dynamics observed in this reference case corresponds to the transient leading to the establishment of the flow in the aerofoil cascade and in the downstream domain. It is interesting to examine the vorticity field in the downstream flow shown in figure 6 in the form of successive maps. The flow is initialized with an axial velocity equal to 4 m s^{-1} everywhere in the computational domain. This does not satisfy the boundary conditions in the cascade and there is an initial adjustment of the flowfield during a short period of

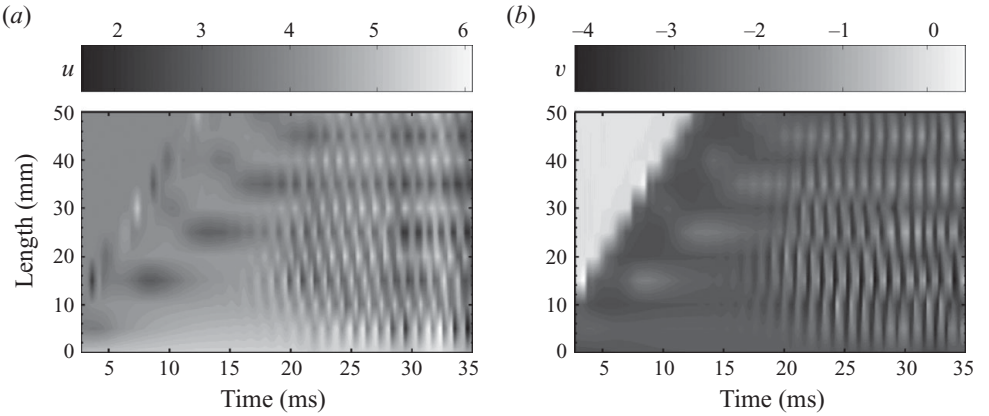

FIGURE 7. Space–time diagrams of velocity components beyond the aerofoils cascade. These diagrams are obtained with raw velocity signals extracted from numerical simulations along straight lines downstream the cascade. Units of the colorbar are m s^{-1}. (*a*) u velocity component. (*b*) v velocity component.

time. A starting vortex is then shed from the trailing edges to satisfy Kelvin's theorem. The circulation in each vortex is opposite to that which develops around each blade. This can be seen at $t = 0.45$ ms in figure 6. One distinguishes a vortex shed at the extremity of each trailing edge. This intense starting vortex is generated to satisfy the conservation of circulation in the flow as expected from Kelvin's theorem. From $t = 2.25$ to $t = 11.25$ ms, this primary vortex is convected in the downstream direction and the wake behind each aerofoil expands in both axial and transverse directions. The starting vortex intensity is progressively reduced by viscous dissipation. This vortex is also dissipated by numerical viscosity that is low but non-negligible when the mesh size increases near the domain outlet. Shear layer instability becomes visible at $t = 13.5$ ms. The instability grows up to $t = 18$ ms. The flow then approaches a state which satisfies the Navier–Stokes equations and boundary conditions on the blades and computational domain boundaries. The amplitude of oscillation saturates for larger times $t > 20.25$ ms giving rise to well-established Kármán vortex streets defining a pattern of counter-rotating vortices.

These simulations are carried out at a modest flow velocity and the flow while unsteady remains laminar but features a periodic pattern of vortices generated by wake instability. The mode conversion process is also operating under turbulent flow conditions, a point which is currently investigated with fully 3D simulations of the flow through a swirler. To obtain a fully-turbulent wake downstream the cascade, the inlet velocity should be augmented but this is out of the scope of this study. To make sure that the flow remains laminar, the calculations were carried out for the modulation-free flow over a long period of 50 ms. It was found that the flow did not transition to a turbulent state but continuously featured distinct vortex patterns like those shown in figure 6.

This dynamics is now studied with space–time diagrams describing the temporal evolution of both axial and transverse velocity components u and v along straight lines in the axial direction. Data were recorded at points separated by a distance $\Delta x = 5$ mm over a distance of 50 mm corresponding to five chord lengths and over a time duration of 35 ms. The aim of the space–time diagrams is to highlight the behaviour of the flow on the downstream side of the cascade. Figure 7 shows the

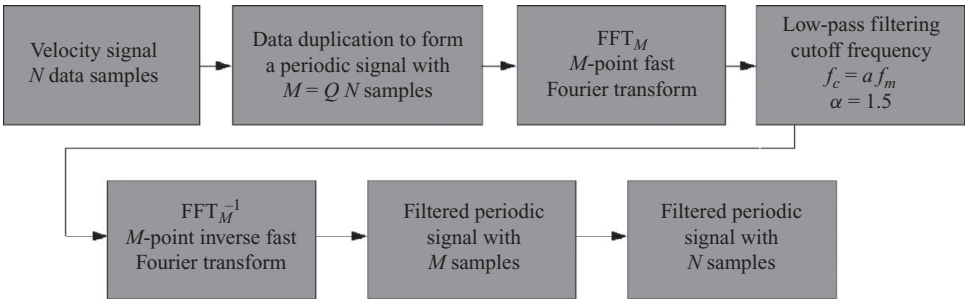

FIGURE 8. Block diagram detailing the filtering procedure of velocity signals.

space–time diagram corresponding to figure 6. The axial and transverse velocity signals are analysed as a function of time in the diagram appearing in figure 7. Figures 7(*a*) and 7(*b*), respectively display the axial $u(x,t)$ and transverse $v(x,t)$ velocity components along this line. From $t=0$ to about $t=20$ ms, one observes in figure 7(*a*) a periodic pattern of alternating high and low velocities convected by the mean flow and corresponding to the shedding and convection of the starting vortex described previously. The second pattern observed is the trace of the wake with a velocity defect as expected. Finally, at $t=18$ ms, a periodic pattern is formed reflecting the convection of vortices in the Kármán streets. The same description applies to the velocity component v displayed in figure 7(*b*). The first pattern is now superposed on a zero-velocity region where no transverse velocity exists before the flow is established in the cascade. The second pattern in this figure corresponds to the trace of the wake and is characterized by a low-velocity region. Beyond $t=18$ ms, one observes a regular pattern associated with the Kármán vortices at a frequency $f=905$ Hz corresponding to a Strouhal number $\mathrm{St}=fl_b/u_\infty=0.25$ based on the blade maximum thickness $l_b=1.1$ mm and the inlet velocity $u_\infty=4\,\mathrm{m\,s^{-1}}$.

3.1. *Data analysis for modulated cases*

The analysis is now carried out both for low and high amplitudes of modulation. The objective is to investigate signal amplitudes and acoustic or convective modes. Some data processing is needed to extract the periodic signals corresponding to the perturbed motion from the complete velocity signal. This can be done by noting that the modulation frequency is well separated from the natural vortex shedding frequency. One may then extract the required information by filtering out the velocity data. The procedure is detailed in the block diagram in figure 8 and consists in applying a fast Fourier transform (FFT) algorithm to the perturbed velocity fields u' and v'. The signal comprising N samples corresponding to three periods is first duplicated Q times to form a longer sequence of $M=Q\ N$ samples. This sequence is then used to get the Fourier transform with an FFT algorithm. The duplication operation applied to the data is used to artificially increase the spectral resolution. The elementary filter size Δf is reduced by a factor $1/Q$. Spectral components corresponding to frequencies exceeding a cutoff value $f_c=\alpha f_m$, f_m being the modulation frequency ($\alpha=1.5$), are then eliminated. This procedure filters out high-frequency components corresponding to vortex shedding in the aerofoil wakes. An inverse FFT is then applied to the result. This process corresponds to a rectangular window in the frequency domain. The transition band is sharp, but the rejection level is moderate. However, by suitably choosing α, one can essentially eliminate the signals associated with vortex shedding yielding the low-pass-filtered velocity disturbances.

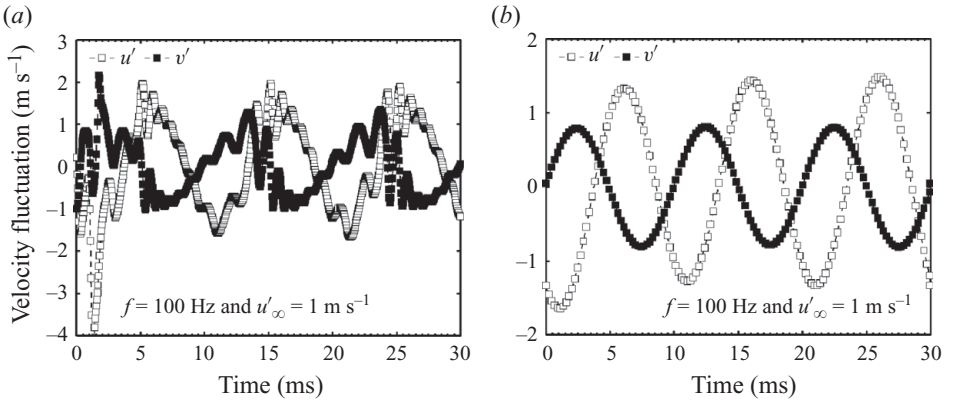

FIGURE 9. Amplitudes of perturbed velocity signals extracted at a distance of 1 chord from the cascade back-end in the computational domain. Data are obtained for an inlet velocity modulation $u'_\infty = 0.1\,\mathrm{m\,s^{-1}}$ with $f = 100\,\mathrm{Hz}$. (a) Raw signal. (b) After low-pass filtering.

One can then investigate the evolution of the phase shift between both perturbed velocity signals u' and v'.

This is obtained by calculating the cross-power spectral densities of the filtered velocity signals at discrete points separated by regular intervals of 5 mm along a line perpendicular to the cascade. The phase difference between the signals is deduced from the complex value of the cross-power spectral density calculated at the modulation frequency f_m. The reference used to establish this phase evolution is the axial velocity signal u' measured at the cascade trailing edge located at $x = 0\,\mathrm{mm}$.

The starting point of the acoustically modulated cases is a mean flow consisting of the flow over an aerofoil with a well-established Kármán vortex street. The flow is unsteady and laminar. After an initial transient of about one period, it is well established and periodic as can be checked by recording signals at various points in the domain. The first period in the numerical simulation is not taken into account in the analysis because the flow is transient. After this initial period, results can be analysed. The mean flow can then be obtained by summing over time to eliminate oscillations associated with vortex shedding from the blade trailing edges.

Typical axial and azimuthal velocity signals are displayed in figure 9. These signals feature a high-frequency component corresponding to the periodic fluctuation associated with alternating vortices in the wakes and a low-frequency component induced by the flow modulation. This last component is extracted by the low-pass filtering method described in figure 8.

3.2. *Low amplitude modulation*

Two frequencies of modulation are investigated $f = 60$ and $f = 100\,\mathrm{Hz}$ at a low forcing amplitude. This is used to validate the theoretical model derived in the linear approximation. The amplitude of the signals and the phase relation between axial and transverse velocity perturbations are specifically considered.

3.2.1. *Signal amplitudes*

Figure 10 displays amplitudes of velocity perturbations u' and v' at a distance of 1 chord from the cascade back-plane. Subfigures (a) and (b), respectively correspond to modulations at $f = 60$ and $f = 100\,\mathrm{Hz}$. In both cases, the amplitude of the relative transverse velocity fluctuation v' is slightly lower than the relative axial velocity

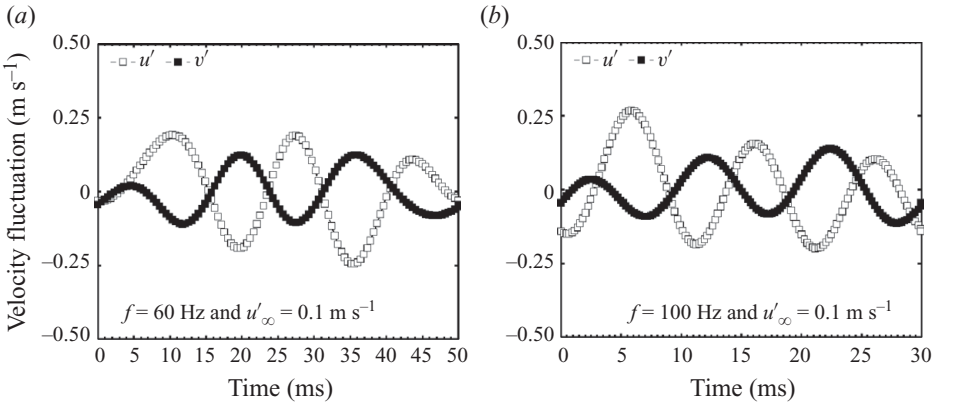

FIGURE 10. Filtered amplitudes of perturbed velocity signals extracted at a distance of 1 chord from the cascade back-end in the computational domain. Data are obtained for an inlet velocity modulation $u'_\infty = 0.1\,\mathrm{m\,s^{-1}}$. (*a*) $f = 60\,\mathrm{Hz}$. (*b*) $f = 100\,\mathrm{Hz}$.

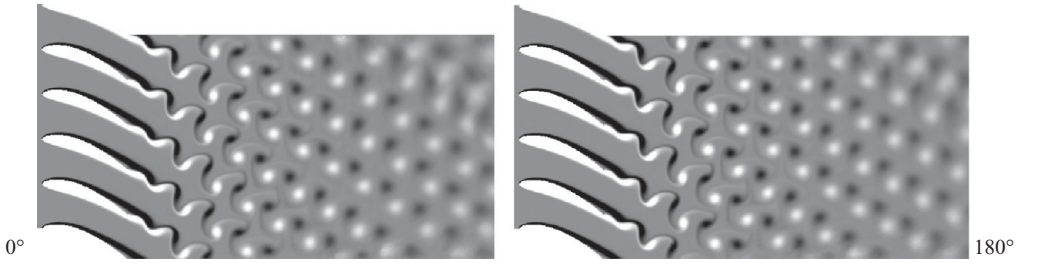

FIGURE 11. Vorticity fields of the flow with an acoustic modulation of amplitude $u'_\infty = 0.1\,\mathrm{m\,s^{-1}}$ at the inlet and for a frequency $f = 100\,\mathrm{Hz}$. The maximum level of vorticity 5000 s^{-1} is in black while the minimum level −5000 s^{-1} is in white.

disturbance u'. This is close to what was predicted analytically. One also finds that the amplitudes of the two signals vary as a function of time indicating that a certain amount of reflection takes place at the computational domain outlet.

3.2.2. *Acoustic and convective mode*

The analysis of vorticity fields is carried out by examining figure 11 presented for $f = 100\,\mathrm{Hz}$ and for two phases in the cycle 0° and 180°. Over one cycle of modulation, one finds that fully developed Kármán vortice streets are established in the aerofoil wakes. The global behaviour is identical for each phase of the cycle: the thickness of the boundary layers around the aerofoil remains almost constant with very small variations, the frequency of vortex shedding is also constant. It is difficult to identify a periodic pattern corresponding to the imposed modulation frequency $f = 100\,\mathrm{Hz}$ for an input level equal to $u'_\infty = 0.1\,\mathrm{m\,s^{-1}}$. These results indicate that with a low input level, it is not possible to detect the vortical mode associated to the modulation frequency because the amplitude of this mode is too low compared to the amplitude of the high-frequency Kármán vortices formed in the blade row wakes.

Results of the data filtering are plotted in figure 12 for two modulation frequencies $f = 60$ and $f = 100\,\mathrm{Hz}$ and for a small perturbation level $u'_\infty = 0.1\,\mathrm{m\,s^{-1}}$. The figure gathers the phases determined with signals extracted from numerical simulations at 60 and 100 Hz, respectively in (*a*) and (*b*). It serves to identify the two types of

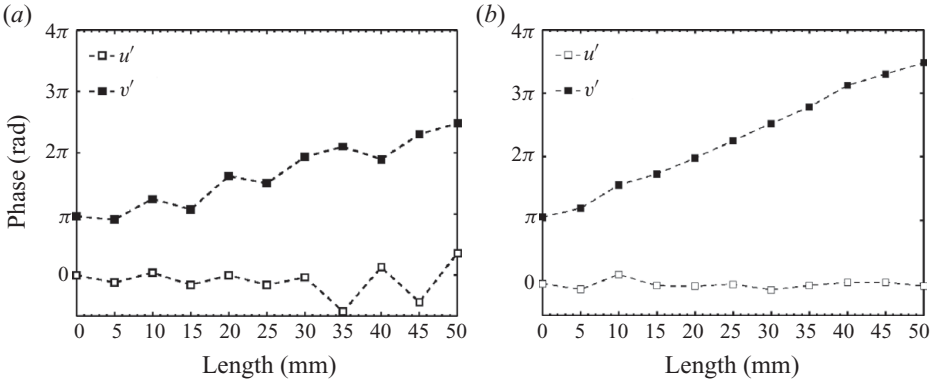

FIGURE 12. Evolution of the phase shift between relative fluctuations of velocity u' and v' in the linear regime. Data are extracted from numerical simulations for a modulation amplitude equal to $u'_\infty = 0.1\,\mathrm{m\,s^{-1}}$. (*a*) $f = 60\,\mathrm{Hz}$. (*b*) $f = 100\,\mathrm{Hz}$.

waves propagating in the downstream flow. The axial velocity disturbance has an essentially constant phase and it is acoustic. The phase shift is negligible because this wave propagates over a small distance at the speed of sound. One can also say that the phase shift is small because the distance is a small fraction of the wavelength. The transverse disturbance is convective as the phase shift increases linearly with distance and frequency and is inversely proportional to the mean axial flow velocity: $\Delta\varphi = 2\pi f x/\overline{u}$.

The transverse perturbations v' are out of phase with axial velocity fluctuations u' at the trailing edge location as expected from linear theory $v'_2 = \tan\overline{\theta}_2 u'_2$ (here, $\tan\overline{\theta}_2$ is negative). Results obtained at $f = 60\,\mathrm{Hz}$ feature some spurious oscillations which are less visible at $f = 100\,\mathrm{Hz}$. This may be attributed to the filtering procedure which does not fully eliminate the high-frequency components. As the relative forcing amplitude is weak ($u'_\infty/u_\infty = 0.025$), the perturbation signal is low and it is affected by residual high-frequency fluctuations. Oscillations are more visible on the acoustic velocity component near the computational domain outlet where some reflections have already been mentioned. These differences do not, however, scramble the general trend. It will be seen below that results can significantly be improved by increasing the modulation level.

3.3. *High amplitude modulation*

We now examine the dynamics of the modulated flow induced by an intense acoustic wave with an amplitude $u'_\infty = 1\,\mathrm{m\,s^{-1}}$ at the inlet of the domain. This case is explored for the same modulation frequencies $f = 60$ and $f = 100\,\mathrm{Hz}$. Amplitudes of velocity components u' and v' are investigated and the acoustic to convective mode conversion mechanism is highlighted with space–time diagrams.

3.3.1. *Signal amplitudes*

The amplitude of velocity signals in the downstream flow are extracted from the numerical fields of u and v. The mean velocity is subtracted to get the fluctuations u' and v'. The low-pass filtering procedure described previously is used to separate the periodic coherent motion due to the modulation. This process is first applied at a point located at a distance of 1 chord from the cascade back plane. Signals are plotted in figure 13 for the two modulation frequencies. One finds that the ratio of amplitudes $|v'|/|u'|$ is close to 0.5 for both frequencies. This is in agreement with

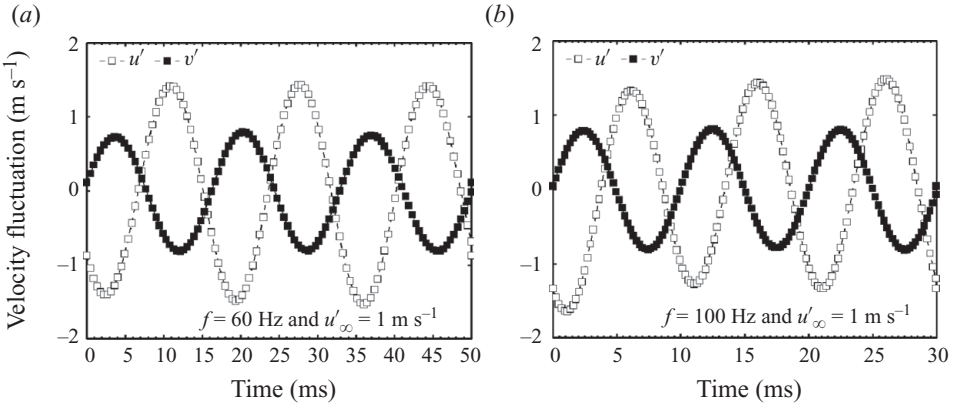

FIGURE 13. Filtered velocity signals extracted from the simulations at 1 chord length downstream of the aerofoil trailing edge for an inlet velocity modulation $u'_\infty = 1\,\mathrm{m\,s^{-1}}$. (*a*) $f = 60\,\mathrm{Hz}$. (*b*) $f = 100\,\mathrm{Hz}$.

analytical predictions obtained in § 2 which give a value $|v'|/|u'| = |\tan\overline{\theta}_2| = 0.47$ for a trailing edge angle $\overline{\theta}_2 = 25°$.

It is also found that the fluctuation amplitude $u' \simeq 1.2\ \mathrm{m\,s^{-1}}$ is greater than that of the incident wave amplitude $u'_\infty = 1\ \mathrm{m\,s^{-1}}$. This is because the axial flow is accelerated due to the presence of the wakes in which the axial velocity is reduced.

3.3.2. *Acoustic and convective modes*

The dynamics of the flow field is now investigated by examining the vorticity fields over one cycle of excitation shown in figure 14. The first phase at 0° shows the classical vortex shedding beyond the aerofoil followed by an intense vortex pair. These two vortices are then convected by the mean flow. At 60°, a new vortex pair is formed at the trailing edge of each aerofoil. This induces an increase of the boundary layer thickness on the suction side near the trailing edge. At 180°, this pair is shed and convected by the mean flow. In the remaining part of the cycle, the classical high-frequency vortex shedding also present in the non-modulated case prevails.

One can now investigate the flow dynamics with space–time diagrams. It is again necessary to filter out velocity components corresponding to the vortices formed in the aerofoil wakes. This is accomplished by applying the method described previously. Because the frequency associated with the Kármán vortices is much larger than the modulation frequency, the corresponding velocity components can be filtered out. It is then possible to extract the coherent motion corresponding to the modulation frequency. Space–time diagrams are obtained for three time periods for both frequencies such that the total time observed is 50 ms at $f = 60\,\mathrm{Hz}$ and 30 ms at $f = 100\,\mathrm{Hz}$.

For the modulation frequency $f = 60\,\mathrm{Hz}$, the space–time diagram is shown in figure 15. The axial velocity fluctuation u' is plotted in figure 15(*a*) while the transverse fluctuation velocity v' is displayed in figure 15(*b*). For the axial velocity, one finds a pattern of alternating black and white vertical stripes. This means that the propagation of axial velocity perturbations is nearly instantaneous indicating that propagation takes place at the speed of sound. For the transverse velocity component, the white and dark stripes are inclined indicating that this component is convected by the flow. It it interesting to extract the convective velocity u_{cv} which can be deduced by estimating the slope of the stripes $a = \Delta l/\Delta t \simeq 3.7\ \mathrm{m\,s^{-1}}$. This value is close to

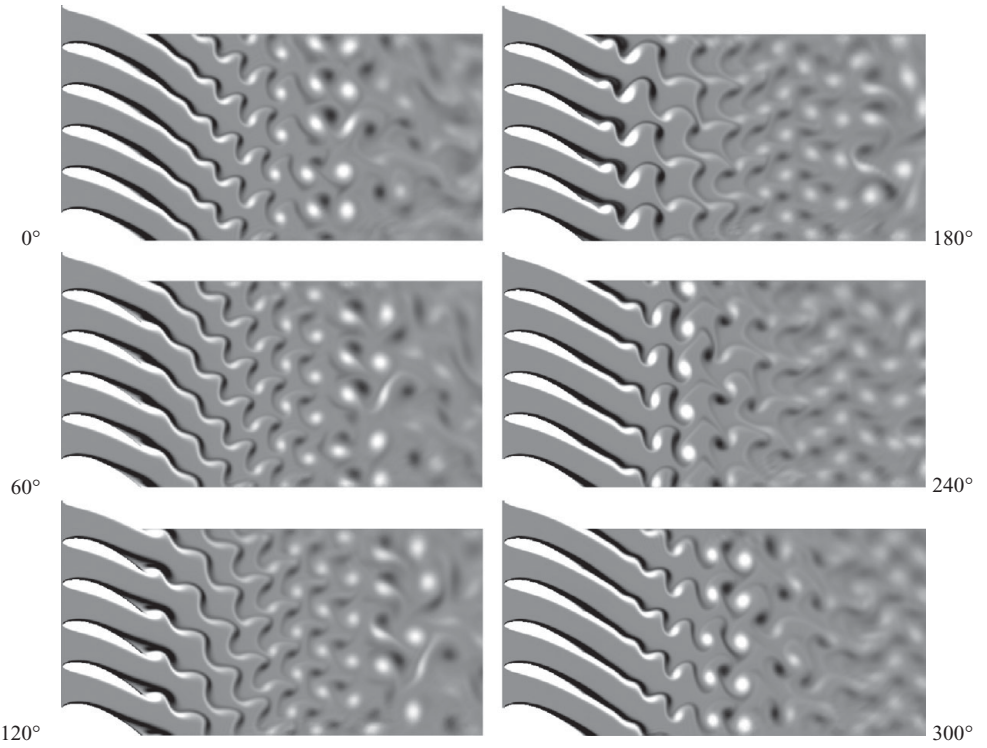

FIGURE 14. Vorticity fields of the flow with an acoustic modulation of amplitude $u'_\infty = 1\,\mathrm{m\,s^{-1}}$ at the inlet and for a frequency $f = 100\,\mathrm{Hz}$. The maximum level of vorticity 5000 $\mathrm{s^{-1}}$ is in black while the minimum level -5000 $\mathrm{s^{-1}}$ is in white. The corresponding time (milliseconds) of each simulation is indicated near each field. The flow is established in three stages: emission of a starting vortex, destabilization of the aerofoil wakes due to a shear instability and fully developed Kármán vortex street.

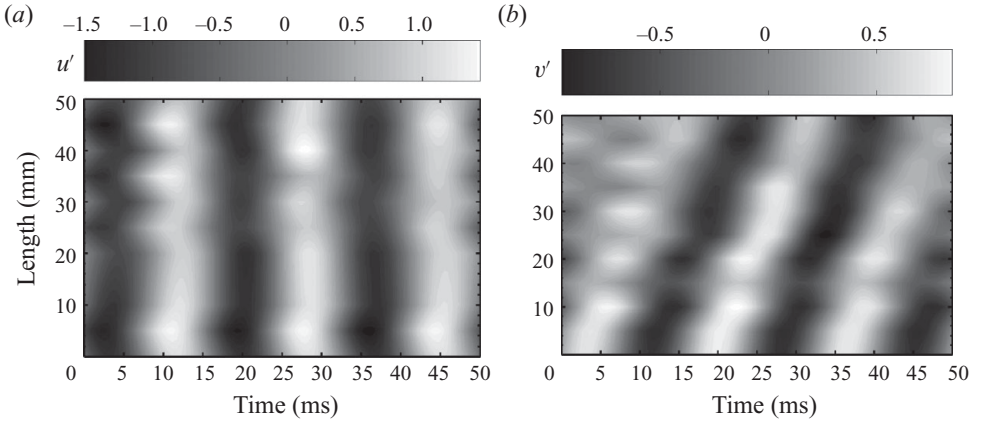

FIGURE 15. Space–time diagrams of fluctuating velocity components beyond the aerofoils cascade for a modulation frequency $f = 60\,\mathrm{Hz}$ and an amplitude equal to $u'_\infty = 1\,\mathrm{m\,s^{-1}}$. These diagrams are obtained by filtering raw velocity signals extracted from numerical simulations along a straight line downstream the cascade and each 5 mm over three time periods. Units of the grey scale are $\mathrm{m\,s^{-1}}$. (*a*) Axial fluctuation u'. (*b*) Transverse fluctuation v'.

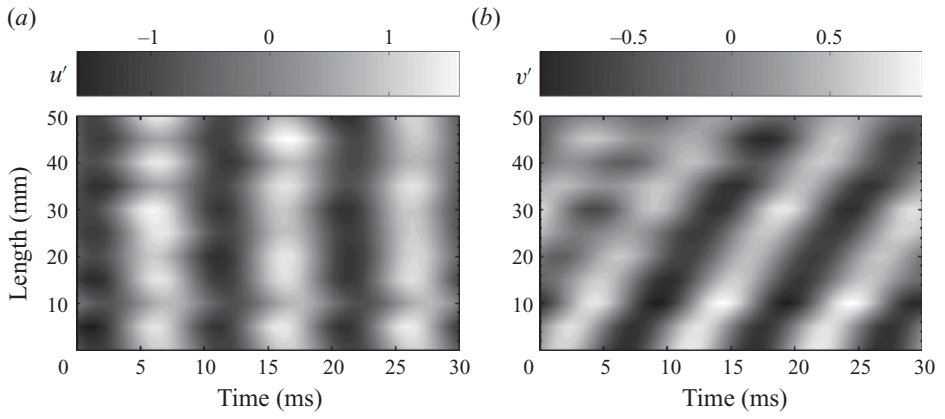

FIGURE 16. Space–time diagrams of fluctuating velocity components on the downstream side of the cascade for a modulation frequency $f = 100\,\mathrm{Hz}$ and an amplitude equal to $u'_\infty = 1\,\mathrm{m\,s^{-1}}$. Theses diagrams are obtained by filtering raw velocity signals extracted from numerical simulations on a straight line downstream the cascade and each 5 mm over three time periods. Units of the grey scale are $\mathrm{m\,s^{-1}}$. (*a*) Axial fluctuation u'. (*b*) Transverse fluctuation v'.

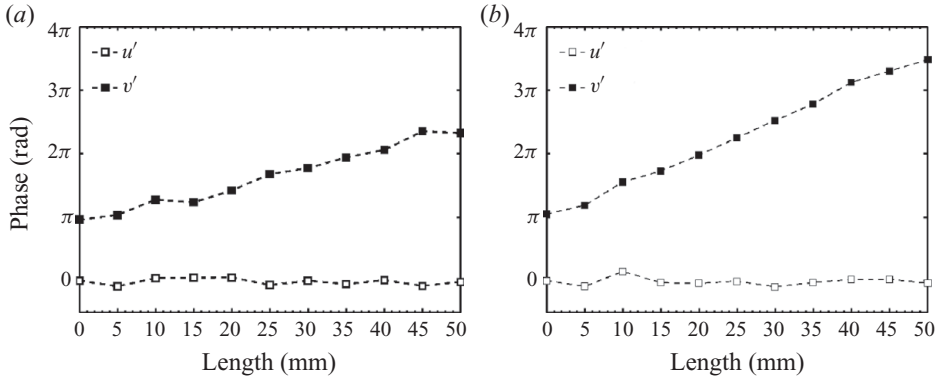

FIGURE 17. Evolution of the phase between axial and transverse velocity perturbations u' and v'. Data are extracted from numerical simulations for a modulation amplitude equal to $u'_\infty = 1\,\mathrm{m\,s^{-1}}$. (*a*) $f = 60\,\mathrm{Hz}$. (*b*) $f = 100\,\mathrm{Hz}$.

the flow velocity $u_\infty = 4\,\mathrm{m\,s^{-1}}$ imposed at the numerical domain inlet. These space–time diagrams confirm that axial and transverse velocity perturbations, respectively propagate at the speed of sound and at a convective velocity as predicted by the analytical model derived in § 2.

A similar analysis can be carried out for a modulation frequency $f = 100\,\mathrm{Hz}$. The corresponding space–time diagrams given in figure 16 are quite similar to those examined previously. Note that the time scale in figures 15 and 16 is slightly different. One can also determine the convective velocity of transverse velocity perturbations with $a = \Delta l/\Delta t = 4\,\mathrm{m\,s^{-1}}$ which is again equal to the inlet flow velocity u_∞. The phase shift between the two velocity components is shown in figure 17. In this case too, the phase evolves in a nearly linear fashion with respect to distance and is essentially proportional to the modulation frequency and inversely proportional to the convection velocity. At the origin, the phase shift is equal to π as expected for a situation where the trailing edge angle $\overline{\theta}_2$ is negative.

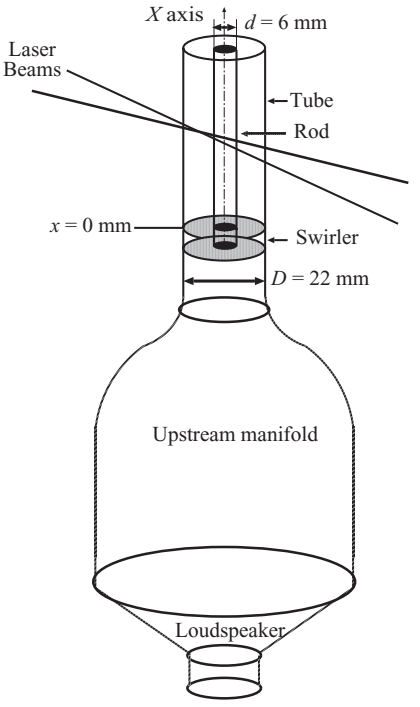

FIGURE 18. Experimental set-up used to determine velocity signals behind a swirler. Laser beams of the laser Doppler velocimeter are used to measure the axial and azimuthal velocity signals each 5 mm over a 50 mm range downstream the swirler. The first measurement point is acquired 17 mm downstream this device due to limitation in optical access.

4. Experiments on a ducted swirler

It is now interesting to see if the previous features can be retrieved experimentally. This is accomplished in a cylindrical configuration where the flow is set in rotation by an axial swirler. This choice is made because experiments are easier to perform in an axisymmetric system. Admittedly, a cascade experiment might have been more consistent with the numerical simulation. However, since we intend to characterize a mechanism, the change in configuration is reasonable.

4.1. *Experimental set-up*

The experimental set-up is sketched in figure 18. The system comprises three elements: a loudspeaker, a convergent unit and a tube containing a swirler. The flow injected at the base of the convergent unit from two orifices diametrically opposed traverses a honeycomb to break the largest turbulent scales and produce a laminar flat velocity flow profile on the upstream side of the swirler. The gas is convected through the swirler, which imparts a rotating motion to the flow. The swirling flow obtained in this way evolves in an annular tube made of quartz. A rod is located at the centre of the tube in this experiment.

The swirler comprises eight vanes periodically spaced. The blades are formed by NACA 8411 profiles and their stagger angle with respect to the axial direction is 45°. Upstream and downstream views of the swirler are displayed in figure 19.

A laser Doppler velocimeter is used to measure the velocity signals in the axial and azimuthal directions. The data are recorded at 5 mm intervals on a vertical line located in the middle of the section between the tube and the rod. This set-up was also used

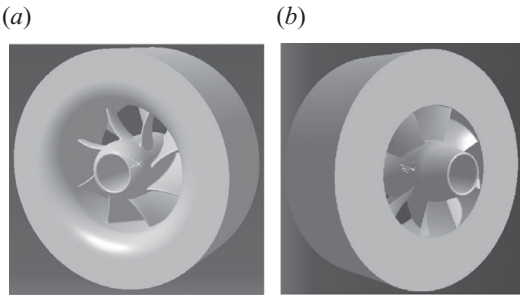

FIGURE 19. Swirler geometry used in the experiment. (*a*) Upstream side. (*b*) Downstream side.

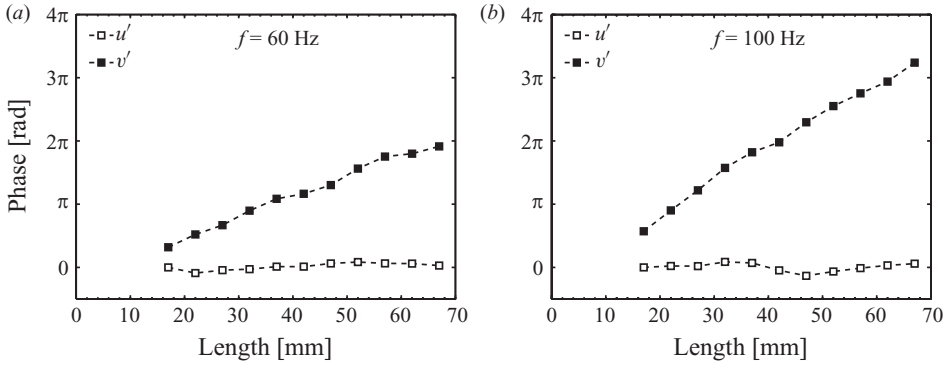

FIGURE 20. Experimental phase shift evolution of axial and azimuthal velocity components u' and v' for two modulation frequencies. Data are recorded from 17 to 67 mm due to limitations in optical access downstream of the swirler. The swirler backplane is located at $x = 0$ mm. (*a*) $f = 60$ Hz. (*b*) $f = 100$ Hz.

in experiments on combustion dynamics reported by Palies *et al.* (2009) and by Palies *et al.* (2010*a*). The bulk velocity in the tube is $U_b = 2.67\ \mathrm{m\,s^{-1}}$ and the fluctuation level of the axial velocity disturbance was measured downstream the swirler, at a distance of 17 mm from the swirler backplane, and it is equal to $u'_{rms}/U_b = 0.5$.

4.2. *Results*

Results gathered from measurements are plotted in figure 20 in the form of phase evolutions for the velocity signals $u(x, t)$ and $v(x, t)$ for two modulation frequencies $f = 60$ and $f = 100$ Hz. One immediately observes that the phase of the axial velocity signal u' is nearly constant when the distance from the swirler increases. This indicates that axial disturbances propagate at a high phase velocity that can only be the speed of sound. An azimuthal component is detected by the laser Doppler velocimeter and this velocity component v' features a phase which varies linearly with distance from the swirler. This reflects the convective character of azimuthal perturbations originating from the swirler blades trailing edges. Using the slope of the phase function, it is possible to determine the convection velocity which is found to be $u_{cv} = 3.05\ \mathrm{m\,s^{-1}}$ for $f = 60$ Hz and $u_{cv} = 3.19\ \mathrm{m\,s^{-1}}$ for $f = 100$ Hz. These two values are of the order of the bulk velocity in the channel indicating that azimuthal perturbations created at the swirler are essentially transported by the flow. It is also worth noting that the phase difference at the aerofoil trailing edges $x = 0$ mm coincides with the theoretical prediction $\Delta\varphi \simeq 0$ by extrapolating the phase curve (black square symbols) to zero.

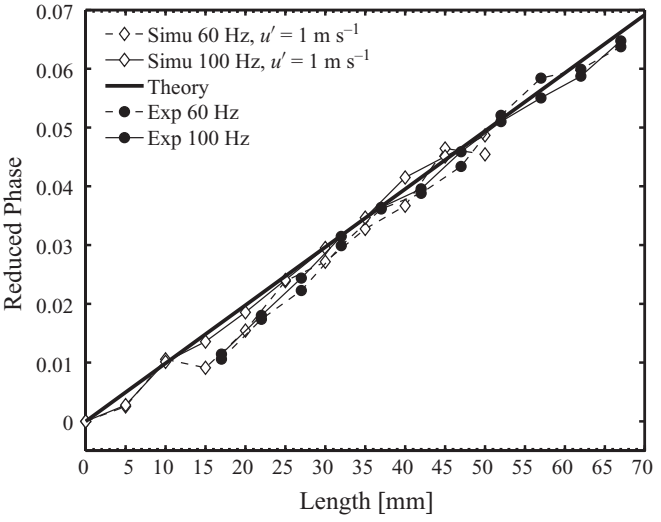

FIGURE 21. Comparison of simulations, theory and experiments with the reduced phase as a function of the length. Results of simulations indicate that the phase shift at the cascade trailing edge plane is equal to $\varphi_0 = \pi$ because of the negative value of the blade trailing edge angle. Results of experiments indicate that $\varphi_0 \simeq 0$ at the swirler backplane.

5. Comparison between theory, numerical simulations and experiments

Analytical results, numerical simulations and experiments are now compared in figure 21. Black symbols correspond to experiments while open markers pertain to numerical predictions. The horizontal axis indicates the distance from the swirler backplane where velocity signals are analysed to determine the phase shift. Measurements are carried out at points separated by an interval of five millimetres. The evolution of the phase shift between u' and v' is specifically examined. It is interesting to introduce a reduced phase to collapse the experimental data and numerical results and compare with theory. This can be accomplished by multiplying the phase by the convection velocity u_{cv} and dividing by the frequency f:

$$\varphi^* = (\varphi - \varphi_0)\frac{u_{cv}}{2\pi f}, \tag{5.1}$$

where φ_0 is the phase between axial and azimuthal velocity signals at the cascade back-plane in 2D or at the swirler in 3D and is respectively equal to $\varphi_0 = \pi$ and $\varphi_0 = 0$. The reduced quantity is plotted in figure 21 as a function of distance from the cascade (simulations) and from the swirler backplane (experiments). One finds that numerical simulations and experimental data closely match theory confirming that the transverse perturbation is well described by the model. Experimental results are in agreement with simulations in that the phase is found to be proportional to frequency and distance and inversely proportional to a convection velocity. The convective velocity is close to the mean flow velocity. Numerical simulations also agree with theoretical predictions of this phase shift. There are, however, minor differences in the phase determined experimentally which are most probably due to the fact that the swirler blades have a variable angle at the trailing edge. This result can be used to predict the phase of the transverse or azimuthal velocity perturbations with respect to incident acoustic disturbances but this requires an estimate of u_{cv} which can be taken equal to the mean flow velocity.

6. Conclusion

The major point of this study is that swirler units used to set a flow rotation act as a mode conversion element. When acoustic waves impinge on a swirler unit, they generate an azimuthal velocity perturbation. When the flow is acoustically perturbed, interactions with a swirler or an aerofoil cascade generate an azimuthal velocity disturbance (in the swirler case) or a transverse velocity disturbance (in the 2D cascade configuration). The main characteristics of this disturbance are documented in this article. Theory, simulation and experiments are used to show that this wave is convected by the flow. The theoretical model based on actuator disk theory provides an estimate of the amplitude of this wave and links its relative level to the relative axial velocity disturbance. It is then demonstrated that this mode conversion process is retrieved from numerical simulations of the flow in a 2D cascade and that the azimuthal velocity disturbance is observed in experiments on an axisymmetric configuration. It can be concluded that the conversion process will have a profound effect on the dynamics of the flow downstream of the swirler and that the combination of axial and azimuthal velocity perturbations will modulate the rate of rotation of the flow. This, in turn, will affect the downstream flow by changing the rate of rotation of the flow. Now, it is known that most practical combustors like those found in jet engines or gas turbines use swirlers to stabilize combustion. The dynamics of the flow will be influenced by the process described in the present article. It has been shown in a recent study of swirling flame dynamics that the upstream flow dynamics plays a central role. The present study focuses on this point and documents this fundamental process with a combination of theory, numerical simulation and experimentation.

The authors wish to thank the anonymous reviewers for their helpful comments. This work was granted access to the HPC resources of CCRT/CINES/IDRIS under the allocation 2009-x2010020164 made by Grand Equipement National de Calcul Scientifique (GENCI). This study is part of the MICCA project supported by the French Research Agency: Agence Nationale de la Recherche. Contract number ANR-08-BLAN-0027-01. The authors also wish to thank A. Scarpato, PhD student at EM2C, for his help in post-processing data.

REFERENCES

Baillot, F., Durox, D. & Prudhomme, R. 1992 Experimental and theoretical study of a premixed vibrating flame. *Combust. Flame* **88** (2), 149–168.

Bake, F., Richter, C., Muhlbauer, B., Kings, N., Rohle, I., Thiele, F. & Noll, B. 2009 The entropy wave generator (EWG): a reference case on entropy noise. *J. Sound Vib.* **326**, 574–598.

Birbaud, A. L., Durox, D. & Candel, S. 2006 Upstream flow dynamics of a laminar premixed conical flame submitted to acoustic modulations. *Combust. Flame* **146** (3), 541–552.

Birbaud, A. L., Durox, D., Ducruix, S. & Candel, S. 2007 Dynamics of free jets submitted to upstream acoustic modulations. *Phys. Fluids* **19** (1), 013602.

Bourhela, A. & Baillot, F. 1998 Appearance and stability of a laminar conical premixed flame subjected to an acoustic perturbation. *Combust. Flame* **114** (3), 303–318.

Boyer, L. & Quinard, J. 1990 On the dynamics of anchored flames. *Combust. Flame* **82** (1), 51–65.

Candel, S. M. 1972 Analytical studies of some acoustical problems of jet engines. PhD thesis, California Institute of Technology, Pasadena, CA.

Crow, S. C. & Champagne, F. H. 1971 Orderly structure in jet turbulence. *J. Fluid Mech.* **48** (3), 547–591.

Cumpsty, N. A. 1979 Jet engines combustion noise : pressure, entropy and vorticity perturbations produced by unsteady combustion or heat addition. *J. Sound Vib.* **66** (4), 527–544.

Cumpsty, N. A. & Marble, F. E. 1977*a* The interaction of entropy fluctuations with turbine blade rows; a mechanism of turbojet engine noise. *Proc. R. Soc. Lond.* Ser. **A357**, 323–344.

Cumpsty, N. A. & Marble, F. E. 1977*b* Core noise gas turbine exhausts. *J. Sound Vib.* **54** (2), 297–309.

De Soete, G. 1964 Etude des flammes vibrantes – application a la combustion turbulente. *Revue de l'Institut Francais du Pétrole et Annales du Combustible Liquide* **XIX** (6), 766–785.

Dotson, K. W., Koshigoe, S. & Pace, K. K. 1997 Vortex shedding in a large solid rocket motor without inhibitors at the segmented interfaces. *J. Propul. Power* **13**, 197–206.

Ffwocs-Williams, J. E. & Howe, M. S. 1975 The generation of sound by density inhomogeneities in low Mach number nozzle flows. *J. Fluid Mech.* **70**, 605–622.

Glegg, S. A. L. 1999 The response of a swept blade row to a three-dimensional gust. *J. Sound Vib.* **227** (1), 29–64.

Greitzer, E. M., Tan, C. S. & Graf, M. B. 2004 *Internal Flow – Concepts and Applications*. Cambridge University Press.

Hirsch, C., Fanaca, D., Reddy, P., Polifke, W. & Sattelmayer, T. 2005 Influence of the swirler design on the flame transfer function of premixed flames. In *ASME Paper GT2005-68195, ASME Turbo Expo 2005,* Reno-Tahoe, NV, ASME.

Horlock, J. H. 1978 *Actuator Disk Theory – Discontinuities in Thermo-Fluid Dynamics*. McGraw-Hill International Book Co.

Howe, M. S. 1975 Contributions to the theory of aerodynamic sound, with application to excess jet noise and the theory of the flute. *J. Fluid Mech.* **71** (4), 625–673.

Huang, Y. & Yang, V. 2009 Dynamics and stability of lean-premixed swirl-stabilized combustion. *Prog. Energy Combust. Sci.* **35**, 293–384.

Kaji, S. & Okazaki, T. 1970 Propagation of sound waves through a blade row. Part I. Analysis based on semi-actuator disk theory. *J. Sound Vib.* **11** (3), 339–353.

Koch, W. 1971 On the transmission of sound waves through a blade row. *J. Sound Vib.* **18** (1), 111–128.

Komarek, T. & Polifke, W. 2010 Impact of swirl fluctuations on the flame response of a perfectly premixed swirl burner. *J. Engng Gas Turbines Power* **132** (061053).

Kornilov, V. N., Schreel, K. R. A. M. & de Goey, L. P. H. 2007 Experimental assessment of the acoustic response of laminar premixed Bunsen flames. *Proc. Combust. Inst.* **31**, 1239–1246.

Leyko, M., Nicoud, F. & Poinsot, T. 2009 Comparison of direct and indirect combustion noise mechanisms in a model combustor. *AIAA J.* **47** (11), 2709–2716.

Marble, F. E. & Candel, S. M. 1977 Acoustic disturbance from gas nonuniformities convected through a nozzle. *J. Sound Vib.* **55**, 225–243.

Morfey, C. L. 1973*a* Amplification of aerodynamic noise by convected flow inhomogeneities. *J. Sound Vib.* **31** (4), 391–397.

Morfey, C. L. 1973*b* Rotating blades and aerodynamic sound. *J. Sound Vib.* **28** (3), 587–617.

Noiray, N., Durox, D., Schuller, T. & Candel, S. 2009 Mode conversion in acoustically modulated confined jets. *AIAA J.* **47** (9), 2053–2062.

Palies, P., Durox, D., Schuller, T. & Candel, S. 2010*a* The combined dynamics of swirler and turbulent premixed swirling flames. *Combust. Flame* **157** (9), 1698–1717.

Palies, P., Durox, D., Schuller, T., Morenton, P. & Candel, S. 2009 Dynamics of premixed confined swirling flames. *Comptes Rendus Mecanique* **337** (6–7), 395–405.

Palies, P., Schuller, T., Durox, D., Gicquel, L. Y. M. & Candel, S. 2011 Acoustically perturbed turbulent premixed swirling flames. *Phys. Fluids* (in press).

Paynter, G. C. 1997 Response of two dimensional cascade to an upstream disturbance. *AIAA J.* **35** (3), 434–440.

Peake, N. & Kerschen, E. J. 1997 Influence of mean loading on noise generated by the interaction of gusts with a flat-plate cascade: upstream radiation. *J. Fluid Mech.* **347**, 315–346.

Rockwell, D. & Naudascher, E. 1979 Self-sustained oscillation of impinging free shear layers. *Annu. Rev. Fluid Mech.* **11**, 67–94.

Rossiter, J. E. 1964 Wind tunnel experiments on the flow over rectangular cavities at subsonic and transonic speeds. *Tech. Rep.* Aeronautical Research Council, Ministry of Aviation, London.

Sajben, M. & Said, H. 2001 Acoustic-wave/blade-row interactions establish boundary conditions for unsteady inlet flows. *J. Propul. Power* **17** (5), 1090–1099.

Schonfeld, T. & Rudgyard, M. 1999 Steady and unsteady flows simulations using the hybrid flow solver avbp. *AIAA J.* **37** (11), 1378–1385.

Schuller, T., Durox, D. & Candel, S. 2003 A unified model for the prediction of laminar flame transfer functions: comparisons between conical and v-flame dynamics. *Combust. Flame* **134** (1–2), 21–34.

Selle, L., Benoit, L., Poinsot, T., Nicoud, F. & Krebs, W. 2006 Joint use of compressible large-eddy simulation and Helmholtz solvers for the analysis of rotating modes in an industrial swirled burner. *Combust. Flame* **145**, 194–205.

Shanbhogue, S. J., Shin, D. H., Santosh, H., Plaks, D. & Lieuwen, T. 2009 Flame sheet dynamics of bluff body stabilized flames during longitudinal acoustic forcing. *Proc. Combust. Inst.* **32** (2), 1786–1893.

Staffelbach, G., Gicquel, L. Y. M., Boudier, G. & Poinsot, T. 2009 Large eddy simulation of self excited azimuthal modes in annular combustors. *Proc. Combust. Inst.* **32**, 2909–2916.

Wang, S. & Yang, V. 2005 Unsteady flow evolution in swirl injector with radial entry. Part II. External excitations. *Phys. Fluids* **17** (045107).